Chemical Engineering Journal 491 (2024) 152196

Contents lists available at ScienceDirect

Chemical Engineering Journal

journal homepage: www.elsevier.com/locate/cej

4D printed shape memory bismaleimide resin with high storage modulus and low shrinkage rate via second-stage curing

Yuejia Li [a], Fenghua Zhang [a,*], Yanju Liu [b], Jinsong Leng [a,*]

[a] Centre for Composite Materials and Structures, Harbin Institute of Technology (HIT), No.2 Yikuang Street, P.O. Box 3011, Harbin 150080, People's Republic of China
[b] Department of Astronautical Science and Mechanics, Harbin Institute of Technology (HIT), No. 92 West Dazhi Street, PO Box 301, Harbin 150001, People's Republic of China

ARTICLE INFO

Keywords:
Bismaleimide
4D print
Shape memory polymers
Two-stage curing
Reconfigurable
Electrical-driven

ABSTRACT

In recent years, the field of shape memory materials with active deformation capabilities has experienced rapid development. However, bismaleimide, as a widely used structural material in the aerospace industry, has been neglected in the field of shape memory. This work designed a UV-crosslinked network with 1-vinyl-2-pyrrolidone monomer, and prepared 4D printed smart structures based on shape memory bismaleimide resin through UV-assisted DIW printing. 4D printed semi-interpenetrating network polymer materials were obtained through a two-stage UV-thermal curing process, resulted in an increase in the material's glass transition temperature to a maximum of 187.4 °C. The storage modulus was improved to 5229 MPa. More important, we achieved a lowest shrinkage rate (0.21 %) of 4D printed polymer. The composite sandwich structure with electrical-driven shape memory performance was printed by double-sided printing of bismaleimide resin on conductive carbon fabric. 4D printed composite structure realizes in-situ self-blocking secondary curing, deformation process after curing. This significant progress provides a promising prospect for remote controllable and precise driving in the aerospace field.

1. Introduction

Shape memory polymers (SMPs) belong to a distinct category of responsive polymers that can be programmed to temporarily hold a shape and then return to their original form when exposed to specific external stimuli [1–6]. This unique ability makes SMPs noteworthy for their autonomous deformation properties, along with their lightweight, cost-effectiveness, ease of processing, controllable deformation characteristics, and adjustable transition temperatures. Various SMPs have been successfully developed in the past few decades, including polyurethane, polylactic acid, polycaprolactone, epoxy resin, etc [7–9]. However, the glass transition temperature of the above SMPs is around 100 ℃, which is difficult to meet the environmental temperature and structural strength requirements of high-orbit space stations. There is an urgent need to carry out research on SMPs that adapt to space temperature and structure. In the realm of engineering, bismaleimide (BMI) stands out as a prevalent thermosetting material renowned for its superior mechanical attributes, high transition temperatures, excellent heat resistance, and thermal stability, surpassing the qualities of thermoplastic materials. As a result, BMI finds indispensable use in the aerospace sector, particularly in applications such as self-deploying structures and morphing aircraft [10–14]. Due to the high crosslinking degree of BMI resin, it generally does not exhibit shape memory performance and is difficult to adapt to the deformation requirements of material. Currently, there is relatively little research on shape memory BMI resins. It is of great significance to develop the shape memory performance of BMI resin to meet the temperature and environmental requirements of aerospace, while also meeting the deformation, remote driving, and precision manufacturing needs of space station structures. The progress in crafting high-performance thermosetting BMI resins embedded with shape memory capabilities holds substantial research value, paving the way for enhanced SMP applications.

BMI is a high-performance thermosetting resin widely utilized in the aerospace materials sector due to its various benefits. It exhibits similar flowability and moldability to other thermosetting resins but stands out for its self-polymerization at temperatures above 180 ℃, creating a robust three-dimensional network. This crosslinking enhances the material's high-temperature performance, though it can lead to brittleness and low fracture toughness once cured. To address these issues, additive blending with materials like cyanate esters [10,11,15], epoxy resins

* Corresponding authors.
E-mail addresses: fhzhang_hit@163.com (F. Zhang), lengjs@hit.edu.cn (J. Leng).

https://doi.org/10.1016/j.cej.2024.152196
Received 5 March 2024; Received in revised form 29 April 2024; Accepted 11 May 2024
Available online 12 May 2024
1385-8947/© 2024 Published by Elsevier B.V.

[16], or diamines [10,11,17] has been explored. Additionally, co-monomers such as allyl compounds can be copolymerized with BMI to enhance toughness. Diallyl bisphenol A, an early allyl compound used for this purpose, offers cost-effectiveness, good flowability during heating, and compatibility with BMI, improving overall material toughness [18]. Li et al. proposed the synthesis of a diallyl molecule with disulfide bonds, which, upon reaction with BMI and the addition of diamines, achieved a modulus change of 506 times and demonstrated self-healing and shape memory capabilities of the material, laying the foundation for shape memory BMI resin [19].

The concept of 4D printing was initially introduced in 2013, merging SMPs with 3D printing technology to enable printing objects capable of changing shape over time [20]. This advanced manufacturing method can directly mold complex structure without the need for further machining, and the complex structure can undergo active deformation to meet the needs of the deformable structure. Following the successful creation of 4D printed SMP structures, an increasing number of researchers have delved into the exploration of 4D printing utilizing SMPs. As 4D printing technology continues to progress and mature, the benefits of 4D printed SMP structures have become increasingly evident [21–27]. Research has shown that 4D printed SMPs can exhibit various functionalities beyond simple shape memory processes, such as self-folding, self-assembling, and reconfiguration through the use of pre-programmed deformation schemes that define target shape, performance, and function [28–33]. Common methods for 4D printing SMPs include Fused Deposition Modeling (FDM), Stereolithography Apparatus (SLA), Polyjet technology, and Direct Ink Writing (DIW). These 4D printed SMPs have found applications in industries such as aerospace, electronics, robotics, health care, medical devices [34–38]. The evolution of nozzle diameter in DIW printing has facilitated the achievement of 4D printing for nano-scale, as well as micro-scale and macro-scale structures [39]. Factors like printing speed and resolution are crucial in determining the chemical, physical properties, and complexity of materials. Researchers have made significant advancements in this field, such as the nano-scale 3D printing of smart nanocomposites by Kim et al. in 2014 [40], and the micron-scale resolution 4D printing of deformable structures using high-resolution Projection micro-Stereolithography (PμSL) technology by Ge et al. in 2016 [24]. In 2017, Mu et al. achieved nanoscale 4D printing using the DIW method [41]. The development of 4D printers capable of operating at multiple scales – nano, micro, and macro – holds promise for practical applications in biomedical device production [42,43], deployable aerospace structures [44], and shape-shifting photovoltaic solar cells [45,46], driving further progress in the field of SMP 4D printed structures. The 4D printed SMPs commonly do not exhibit conductivity. By mixing conductive particles in printing ink or printing the structure onto conductive materials, a continuous internal conductive network can be formed, resulting in a 4D printed structure with conductive properties. Under electrification conditions, the Joule heating effect is utilized to achieve electrical-driven deformation of SMP composites. 4D printed electrical-driven SMP capable of remote driving, integral taking shape of complex structures, and designable structures.

In this study, we synthesized a printable BMI-based ink, which is fabricated through UV-assisted DIW 4D printing. The material exhibits high modulus and low shrinkage, as well as outstanding shape memory and reconfigurability capabilities. Specifically, the printing process of the BMI resin is achieved by introducing photosensitive molecules and applying UV light. The material is further thermally cured, leading to a two-step curing process that results in a semi-interpenetrating network (semi-IPN). The interweaving of linear and cross-linked molecular chains allows the material to demonstrate superior shape memory effects. The two-step curing process and molecular structure design contribute to the high storage modulus and low shrinkage of the material. By printing a sandwich structure on a conductive substrate and controlling the voltage, the reconfigurable behavior of the composite material, which includes shape memory deformation, in-situ self-blocking electrical-heating secondary curing, and subsequent shape memory deformation, is achieved. This breakthrough establishes a robust foundation for in-orbit printing, and the process of electrical-heating curing and secondary deformation opens up new possibilities for the advancement of deformable structures in the aerospace field.

2. Material and methods

2.1. Materials

4,4′-bismaleimideodiphenylmethane (BDM, 98 %) and 1-Vinyl-2-pyrrolidone (NVP, 99 %) were commercially sourced from Shanghai Macklin Biochemical Technology Co., Ltd, while Diphenyl(2,4,6-trimethylbenzoyl)phosphine oxide (TPO) was obtained from Shanghai Aladdin Biochemical Technology Co., Ltd. All chemicals used in the experiments were of analytical grade and were used without any further purification steps. Conductive carbon fabric HCP330N was bought from Shanghai Jingchong Electronic Technology Development Co., Ltd.

2.2. Synthesis of BMI-based ink

The BDM and 4,4′-diallyloxydiphenyldisulfide (DPS, prepared according to previous work [19]) were mixed in a 1:1 M ratio at 150 °C for 1 h. The resulting oligomer was used as the basic molecule of the ink. The oligomer was cooled to below 70 °C, after which an appropriate amount of NVP is added and stirred evenly. 5 wt% of TPO was then added as a photoinitiator. The NVP molecule was introduced as a diluent to enable the resin to be UV-cured for printing. The resulting resin mixture was used as ink for printing and stored in the dark. The molar ratios of NVP to BDM in the ink were 3:1, 3.5:1, and 4:1, resulting in inks named BMIP-1-R, BMIP-2-R, and BMIP-3-R, respectively. The oligomer and NVP components are miscible, wherein a ratio of 3–4:1 will be suitable for the requirements of straight writing printing.

2.3. Fabrication of printing structures

The process of printing using a bioprinter (4th generation Envisiontec 3D-Bioplotter, Manufacturer Series, Envisiontec GmbH, Germany.) began by filling the ink into the High-Temp Dispensing-Head with a needle inner diameter of 0.4 mm, assembling the syringe onto the printer, and using an extrusion pressure of 0.2–0.3 bar and a temperature of 75–80 °C to print the material onto a flat substrate (aluminum foil or conductive carbon cloth). The printing speed is adjusted to 4–5 mm/s so that the extruded filaments are uniform and continuous, and the printing spacing is adjusted to obtain the desired solid or hollow structure. The layer thickness was set to 0.16 mm and 0.2 mm, and after each layer was printed, a UV lamp (365 nm, 7 W) was used at a distance of 2 mm vertically to cure the printed parts for 1 min. After printing was completed, the aluminum foil and the printed structure were placed together in an oven for curing, with the curing process at 120 °C / 2 h, 180 °C / 2 h, and 200 °C / 1 h, followed by cooling to obtain the printed 3D structure and test samples. The samples in the shape of long strips and dumbbells were printed with a thickness of 1 mm respectively, and the conductive sandwich structure was printed with a thickness of 0.5 mm on both sides of the conductive carbon fabric. The conductive sandwich structure printed on the conductive carbon fabric underwent subsequent electrical-curing. The temperature and time of the electrical-curing process were the same as those of the thermal curing process. However, the electrical-curing process achieved temperature elevation by increasing the voltage. The specific voltage used was dependent on the resistance of the electrically conductive medium.

2.4. Chemical and thermodynamic characterization

Fourier Transform Infrared (FTIR) Spectrometer: FTIR spectra were obtained with a Spectrum Two DGTS instrument from Perkin-Elmer in

MA, USA, fitted with a universal attenuated total reflection (ATR) accessory. This configuration facilitated the examination of molecular vibrations and functional group interactions across a wavelength range of 2000–650 cm^{-1} at a spectral resolution of 4 cm^{-1}.

Rheology Analysis: The rheological properties of the materials were assessed utilizing a TA Instruments Waters LLC Rheometer with a 25 mm diameter parallel plate aluminum setup, where the plate-to-plate distance was maintained at 500 μm. The shear-thinning performance of the printing ink was characterized using the Flow Ramp mode. The test temperature was maintained at 80 °C, and an exponential mode with shear rates ranging from 0.1 1/s to 100 1/s was applied. Additionally, the shear-thinning behavior of the printing ink was characterized using the Flow Peak Hold mode. The test temperature was set at 80 °C, employing a "low-high-low" three-step ramp rate of 0.1 1/s for 120 s, 500 1/s for 30 s, 0.1 1/s for 300 s.

Shrinkage measurement: Rectangular samples with a size of 10 × 10 × 1 mm^3 were used to measure the shrinkage rate of the resins. The material shrinkage was characterized by measuring the dimensional changes of test samples before and after thermal curing. The sample dimensions were measured using a vernier caliper, with the initial length before thermal curing denoted as L_1, and the length after thermal curing denoted as L_2. Shrinkage rate was calculated by Eq. (1). The average size change of the three side lengths were taken as the average shrinkage rate of the resins.

$$Shrinkagerate = \frac{L_1 - L_2}{L_1} \times 100\% \tag{1}$$

Thermal Analysis: Thermogravimetric analysis (TGA) was carried out on a Mettler-Toledo TGA/DSC STARe System in a nitrogen (N2) and air atmosphere. The samples underwent heating from 30 to 800 °C at a speed of 10 °C minute^{-1}. This analytical technique yielded valuable information about the thermal properties and stability of the SMPs. Analysis of weight loss as a function of temperature enabled the characterization of material decomposition and degradation behaviors.

Mechanical Testing: Uniaxial tensile tests were carried out using a Zwick electronic universal material testing machine to evaluate the static mechanical properties. The tests were performed at room temperature (R.T.) with a cross-head speed of 1 mm min^{-1}, following ASTM-D638 Type-V standards for the pristine BMIP-1 to BMIP-3 and BMIP-1-UV to BMIP-3-UV samples.

Swelling Test: The crosslinking density was determined through a swelling test. Initially, approximately 0.2 g of the sample was weighed and denoted as m_1. It was subsequently placed in a suitable amount of either deionized water or toluene. Every once in a while, the sample was gently dried to remove any solvent from the surface, record the quality of the dried sample until there is little change in quality. The final recorded sample mass is the final mass, designated as m_2. The swelling degree was determined using Eq. (2):

$$Swellingdegree = \frac{m_2 - m_1}{m_1} \times 100\% \tag{2}$$

Dynamic Mechanical Properties: Rectangular samples measuring 30 × 4 × 1 mm^3 were assessed for dynamic mechanical properties in tensile mode through Dynamic Thermomechanical Analysis (DMA). The samples were clamped using a tensile mode clamp and subjected to a 3 °C/min heating rate within a temperature range of 30 ℃ to 250 ℃. A pre-strain of 0.05 % and a frequency of 1 Hz were utilized. According to the theoretical evolution equation of rubber elasticity [47,48], the cross-linking density ν_e of the thermosetting resin was calculated by Eq. (3):

$$\nu_e = E/(6RT) \tag{3}$$

where ν_e is the cross-linking density; E is the rubber platform storage modulus of the resin at $T_g + 40$ °C, in units of 0.1 Pa; R is the gas constant, 8.314 J mol^{-1} K^{-1}; and T is the absolute temperature.

2.5. Functional verification

Shape Memory Performance: The SME tests involved visual bending tests, where samples measuring 72 × 10 × 1 mm^3 were folded into a U-shape at a temperature of 240 °C (or 130 °C for BMIP-2-UV samples) and then fixed at room temperature. The fixed angle was recorded as θ_{fix}. After heating to 240 °C (for BMIP-2-UV samples, the temperature was 130 °C), the recovered shape was obtained, and the angle was recorded as $\theta_{recover}$. The time taken for the recovery process was recorded as t.

$$R_f(\%) = \frac{\theta_{fix}}{180} \times 100\% \tag{4}$$

$$R_r(\%) = \frac{180 - \theta_{recover}}{180} \times 100\% \tag{5}$$

Healing Process and Optical Microscopy Imaging: The sample was placed on a heating stage set at 240 °C, and its surface was scratched to a depth of about 0.5 mm using a blade. After the scratch, the sample was quickly cooled, and microscopic photos were taken for analysis. Optical microscope images were taken before and after the healing process. The samples post-healing was designated as BMIP-1-H to BMIP-3-H, respectively. Testing of the healing BMIP-1-H to BMIP-3-H samples was conducted in accordance with ASTM-D638 Type-V standards. The healing rate for each sample was determined by comparing the modulus and elongation at break of BMIP-1-H to BMIP-3-H with the original BMIP-1 to BMIP-3 samples, respectively.

3. Results and discussion

3.1. Ink synthesis and compound structure

Fig. 1(a) illustrates the synthesis process of the ink, where BDM and DPS molecules undergo pre-polymerization followed by an ene reaction. to produce the copolymer as the base molecule of the ink. At this point, a preliminary condensation reaction occured between the double bond on the maleimide ring and the double bond on DPS, forming an oligomer, as shown in the third row of Fig. 1(a). This oligomer acted as the base molecule of ink and served as the part with higher viscosity in the ink, playing a preliminary role in maintaining the printing structure in subsequent steps. NVP molecules are introduced as diluents to adjust the viscosity of the resin to make it suitable for DIW printing. In Fig. 1(b), the ink is printed into shape using DIW assisted by ultraviolet light. The ink is extruded layer by layer onto the platform, accumulating to form a three-dimensional structure. During extrusion, ultraviolet light is used to irradiate the structure on the platform. At this point, the photosensitive NVP molecules in the ink undergo photopolymerization under the action of the photoinitiator TPO, opening double bonds to form linear molecules, while the remainder does not react, placing the ink in a partially cured state. The structure of the UV-cured resin has a certain ability to maintain its shape, allowing the structure to remain unchanged from the printed structure during the subsequent thermal curing process. Subsequently, the partially cured material is heated, causing the remaining BDM and DPS to react, with the bismaleimide ring and double bonds undergoing ene reactions, along with a small amount of bismaleimide ring undergoing radical polymerization, completing the material's reaction.

3.2. Ink performance and UV-Curing sample performance

DIW printing is a method of printing that directly extrudes materials and stacks them into a three-dimensional structure, so the rheological properties of the extruded materials need to be characterized. We characterize the rheological behavior of materials with different formulations through rheological tests, as shown in Fig. 2. We choose the "Flow Ramp" mode to characterize the shear-thinning performance of the materials, indicating the performance when the materials start to

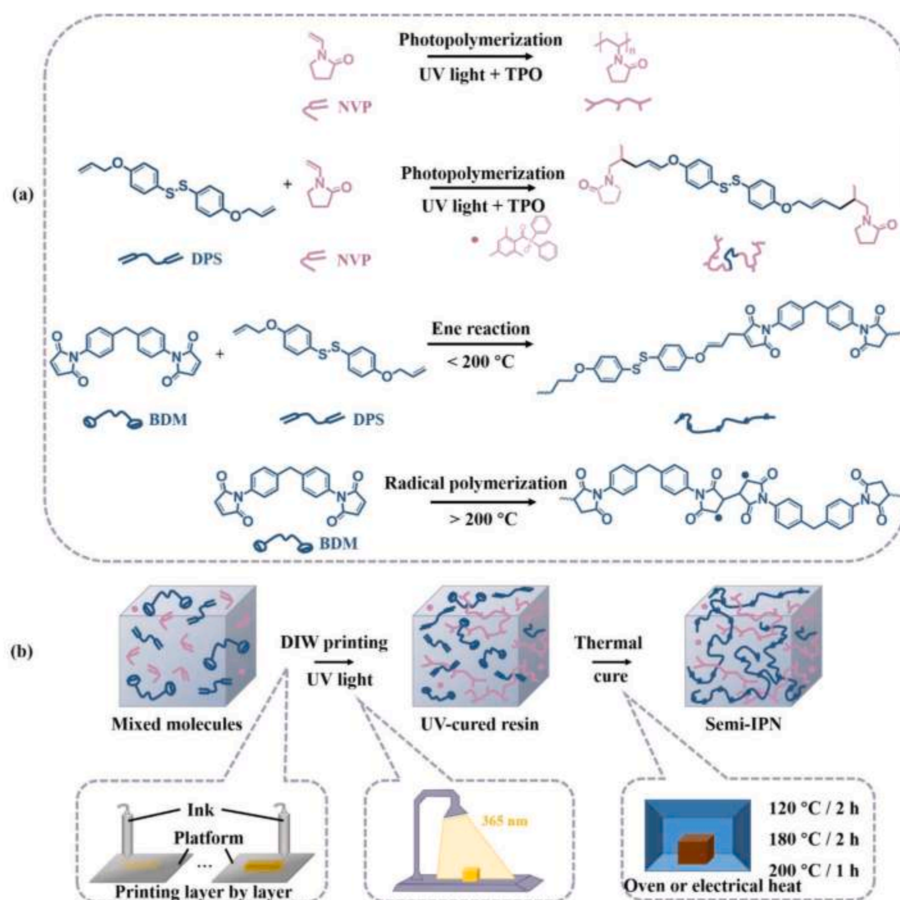

Fig. 1. (a) Molecular diagram illustrating the synthesis process of a semi-IPN, (b) Schematic diagram of the two-step curing process, including images depicting direct writing, photocuring, and thermocuring.

flow, as shown in Fig. 2(a)-(c). Additionally, we choose the "Flow Peak Hold" mode to characterize the thixotropic performance of the materials, as shown in Fig. 2(d)-(f). Fig. 2(a)-(c) show the relationship between the apparent viscosity and shear rate of three types of inks. The specific values of apparent viscosity, shear rate and shear yield strain of the inks were summarized in Table S1. It can be observed that as the shear rate increases, the viscosity of these inks sharply decreases and then gradually stabilizes. All inks exhibit shear-thinning characteristics, making them flow smoothly in the printing nozzles to meet printing requirements. As the content of NVP increases, the shear yield stress of the inks gradually decreases, indicating that NVP can adjust the rheological properties of the BMI inks. The oligomer composed of BDM and DPS has a higher viscosity than that of NVP. When the content of this oligomer is high, the viscosity of the printing ink can be very high, resulting in the printing ink not being able to be extruded from the print needle. When the content of this oligomer is low, the viscosity of the printing ink will be low, causing the printing ink to be unable to maintain the printed structure after extrusion. Fig. 2(d)–(f) depict the low viscosity observed at high shear rates and the high viscosity seen at low shear rates for the three inks. The inks' low viscosity at high shear rates facilitates smooth extrusion from the printing nozzles, while their high viscosity at low shear rates aids in maintaining their shape post-extrusion. This thixotropic behavior enables these inks to maintain their shape fidelity during the printing process, making them suitable for DIW printing.

We characterized the functional groups of the material through FTIR to elucidate the molecular structure and the occurrence of the aforementioned reactions. As shown in Fig. 3(a), the out-of-plane bending vibration peaks of the = C-H bond in the allyl group of DPS are observed at 996 cm^{-1} and 912 cm^{-1}, present in the curve of the DPS molecule, as well as in the UV-cured and thermally cured materials. The out-of-plane bending vibration peak of the = C-H bond in the vinyl group in NVP is observed at 983 cm^{-1}, present in NVP but absent in photocured materials. This is because under conditions of UV exposure, the double bond in NVP opens leading to photopolymerization, resulting in the absence of the vinyl group in the fully photopolymerized material. In BDM, the vibration peak of the maleimide ring in the maleimide ring is observed at 687 cm^{-1}, present in BDM molecules. This vibration peak is also present in photocurable materials, as only the photopolymerization reaction has occurred, and the maleimide rings have not reacted. In thermal-cured materials, the vibration peak of the maleimide ring is absent due to the reaction of the maleimide ring under thermal conditions. The materials obtained at this point consist of a linear polymer (produced by NVP photopolymerization) and a crosslinked polymer (formed by the thermal polymerization of bismaleimide as the backbone). This type of polymer is known as a Semi-Interpenetrating Polymer Network (Semi-IPN). Semi-IPN offers the potential for high modulus, low shrinkage, and shape memory properties in materials.

After photopolymerization of the ink, we discovered that the material that underwent photopolymerization alone exhibited a certain tensile strength. We conducted tensile tests on the photopolymerized material, and the obtained stress–strain curve is shown in Fig. 3(b), while the data for modulus, strength, and elongation are presented in Table S2. It is essential that the photopolymerized material has a certain strength and modulus. In this way, the photopolymerized portion of the material provides support for maintaining the shape of the material during subsequent thermal curing. Otherwise, the printed 3D structure would soften during thermal curing and would not be able to retain its

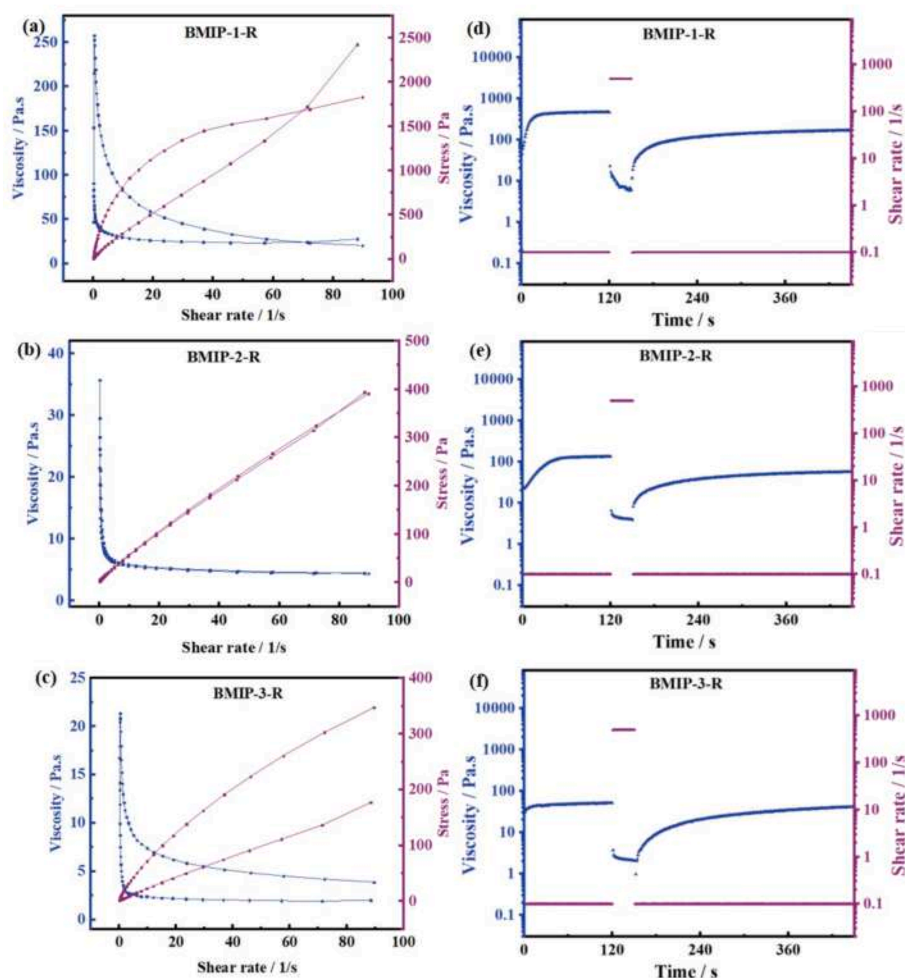

Fig. 2. Rheological behavior of materials with different ratios, (a)-(c) Results of "Flow Ramp" mode; (d)-(f) Results of "Flow Peak Hold" mode.

shape. Furthermore, materials with higher NVP content exhibited higher modulus after photopolymerization. During photopolymerization, only the NVP portion underwent reaction, thus materials with higher NVP content had a higher proportion of reacted components, leading to a higher modulus. Furthermore, we observed that the photopolymerized material also demonstrated shape memory effect and characterized it. The DMA curves for differently ratios of photopolymerized samples are shown in Fig. 3(c). The DMA tests revealed significant changes in storage modulus among samples of different compositions. At a low-temperature plateau, the samples displayed a high modulus and a glassy state, while at a high-temperature plateau, the samples showed a low modulus and a rubbery state. The storage modulus of the material sharply decreased between the two plateaus, indicating the presence of a shape memory effect. The peak of the Tan δ curve corresponds to the glass transition temperature (T_g) of the material. Materials with higher NVP content exhibited higher modulus and higher T_g at the low-temperature plateau, similar to the reason for higher tensile modulus in the material. We selected BMIP-2-UV for demonstrating the shape memory performance of photopolymerized materials, and we chose 130 °C as the temperature for inducing shape memory deformation to verify the shape memory effect. Fig. 3(d) illustrates the shape memory cycling process of claw-shaped photopolymerized samples of BMIP-2-UV material. The claw shape was deformed under an applied force at 130 °C, set into a closed position, and retained this shape after cooling to room temperature. Subsequently, when placed on a heating platform, it autonomously unfolded as shown in the figure. Quantitative measurements of the fixed angle and recovered angle of BMIP-2-UV were conducted as shown in Fig. S1(a). Fig. S2(a) depicts the recovery process and time of BMIP-2-UV on the 130 °C heating platform. By comparing the fixed angle with the recovered angle, we calculated the fixation recovery ratio of BMIP-2-UV as presented in Table 1. At this stage, although the material has not fully cured, the photopolymerized polymers already enable the material to have a good shape fixation rate. However, there are some uncured small molecules or oligomers interspersed in the photopolymerized polymers, and due to their lack of "soft segment" and "hard segment" structure, they deform into a temporary shape when the material is fixed into a temporary shape during heating. The presence of these small molecules or oligomers slightly impairs the recovery of the material during the shape recovery process, thereby slightly reducing the recovery rate and decreasing the recovery speed of the material.

3.3. Printing and structure

Different printing parameters will have an impact on the printing results, as shown in Fig. 4. Firstly, by controlling the printing temperature, the forming effect of the ink extrusion can be adjusted, as shown in Fig. 4(a). When the ink temperature is low, the flowability is poor, resulting in single-thread extrusion. As shown in Fig. 4(a)i), the extruded threads appear as clear stripes at a macroscopic level, exhibiting poor adhesion to each other. In contrast, when the ink temperature is high, the flowability is better, and the extruded threads will overlap to some extent, showing better continuity in Fig. 4(a)ii). Therefore, 80 °C was chosen as the printing temperature for the test samples to demonstrate

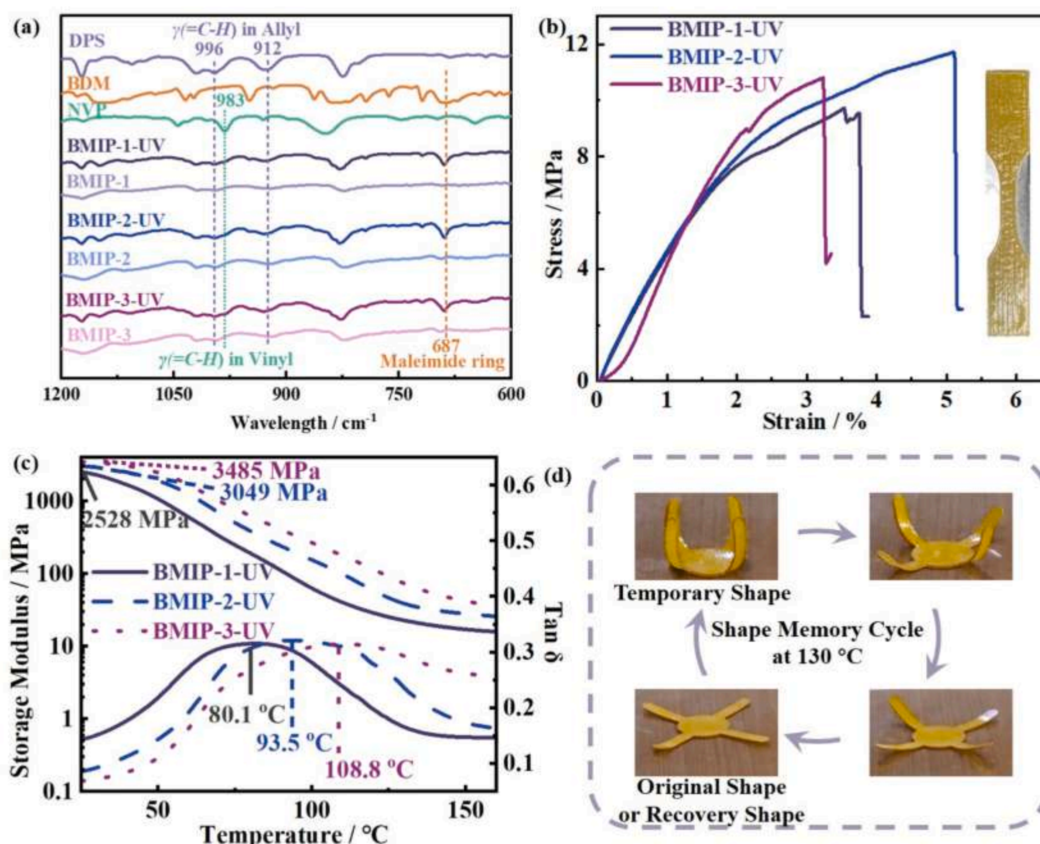

Fig. 3. (a) FTIR spectroscopy of molecules before reaction, materials after photocuring with resin at different ratios, and materials after thermal curing, (b) Tensile curves of photocured samples at different ratios, (c) DMA curves of photocured samples at different ratios, (d) Shape memory cycle of four-claw shape cut from photocured sample BMIP-2-UV.

Table 1
Fixed rate, recovery rate and recovery time of BMIP-2-UV, and BMIP-1 to BMIP-3.

Sample	BMIP-2-UV	BMIP-1	BMIP-2	BMIP-3
Rf [%]	100.0	100.0	100.0	100.0
Rr [%]	97.2	98.8	100.0	100.0.
t [s]	210	180	120	80

satisfactory mechanical properties. The effects of different thread structures printed with BMIP-2 resin by adjusting the printing pattern spacing are shown in Fig. 4(b), which include wide-cross-wave, wave, honeycomb, and line patterns. Secondly, adjusting the printing layer thickness can control the curing effect and printing efficiency, as illustrated in Fig. 4(c). Due to the limited penetration of ultraviolet light, incomplete curing of the ink may occur when the layer thickness is large. As shown in Fig. 4(c-i), using a layer thickness of 0.2 mm for printing can result in uncured parts between layers, leading to structural distortion after thermal curing. Although good curing effects can be achieved with thin layer thickness, printing efficiency is compromised. By adjusting the layer thickness to 0.16 mm, the highest printing efficiency can be achieved while ensuring proper curing, as depicted in Fig. 4(c-ii). Finally, we achieved printing materials on a conductive substrate, as shown in Fig. 4(d). Fig. 4(d-i) illustrates the printing of a conductive sandwich structure, where conductive material is placed on the printing platform for printing and then flipped for a second print to create the conductive sandwich structure. Set the printed structure as a mesh structure with 0/90° lines in staggered rows. Compared to a solid structure, a hollow structure has a better deformation capacity and greater flexibility when being bended. The mesh area also facilitates the heating of the entire structure by the conductive substrate. As evident in Fig. 4(d-ii,iii), the printed structures are clear, and the combination between the printing structure and the conductive layer is well-demonstrated in the top view.

3.4. Thermal and mechanical properties

The thermodynamic properties of thermal-cured resin post-curing are demonstrated in Fig. 5, reflecting the fundamental characteristics of the material. The mechanical properties of the resin are assessed through static tension tests. In Fig. 5 (a), stress–strain curves for various material compositions are illustrated. Static modulus, strength, and elongation at break are derived from these curves and presented in Fig. 5 (b). Specific data are summarized in Table S3. It can be seen that the static modulus of the materials were increased from 497.0-608.7 MPa to 675.6–688.3 MPa, the strength of them were increased from 9.5-11.7 MPa to 16.9–17.2 MPa, and the elongation at break of them were increased from 3.3-5.1 % to 6.9–7.3 %. The static modulus, strength, and elongation at break of the material were all improved to a certain extent. As there are still some small molecules present in the material before thermal curing. After thermal curing, BDM and DPS were reacted, and the mechanical properties of the material were improved. The incremental NVP content corresponds to a slight reduction in the slope of the curves, indicating a marginal decrease in the material's modulus, although not as pronounced as in photocured materials. This phenomenon can be attributed to the elongation of molecular chain segments within the material with higher NVP content. Longer segments exhibit increased flexibility, enhancing the material's deformability and resulting in a lower modulus. As mentioned above, the modulus of photocured materials increases with increasing NVP content, while the

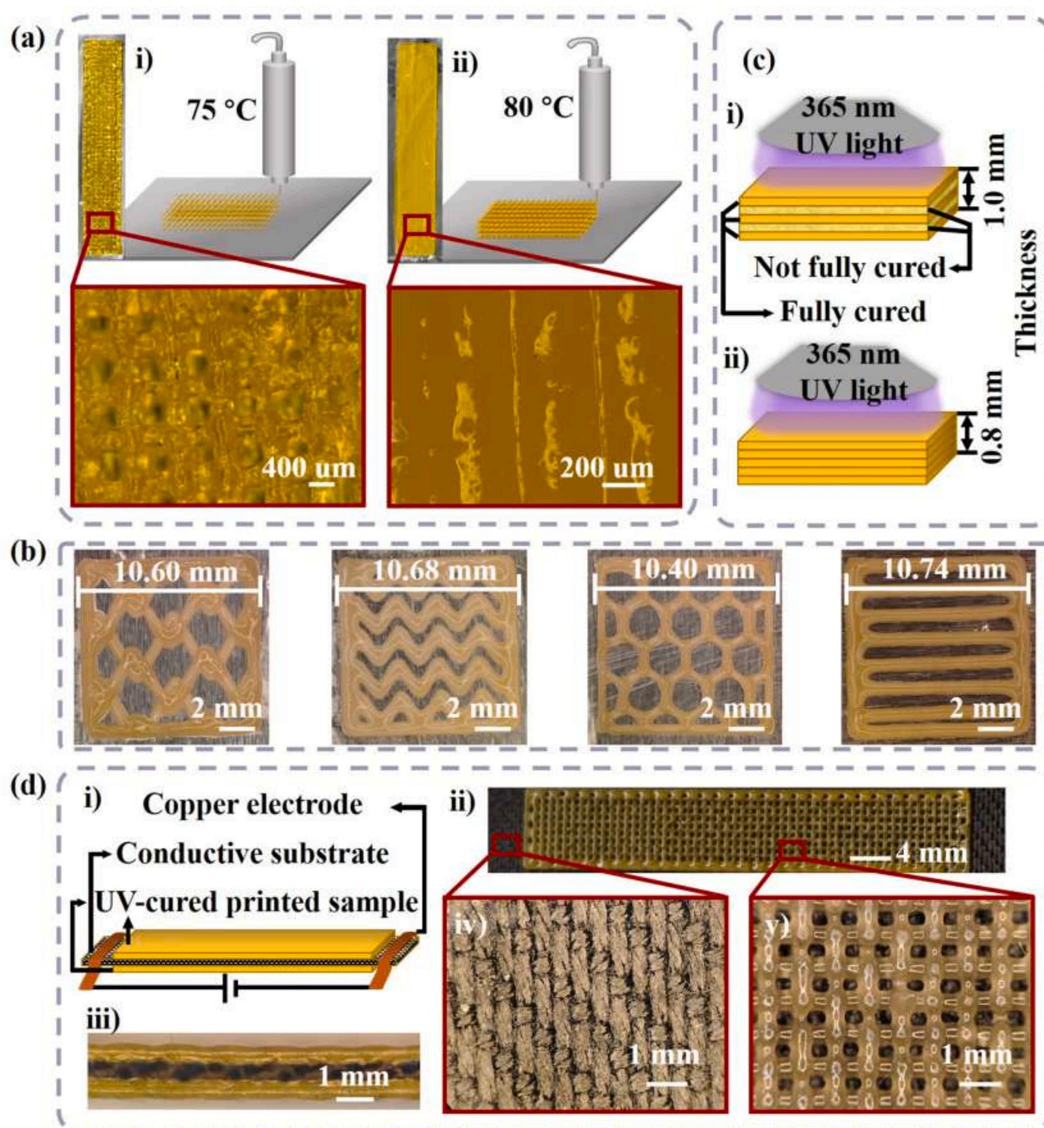

Fig. 4. (a) Comparison of print effects using different temperatures, i) ink temperature at 75 °C, ii) ink temperature at 80 °C; (b) Effects of different printing patterns; (c) Comparison of curing effects of samples with different printing layer thicknesses, i) printing layer thickness of 0.2 mm, ii) printing layer thickness of 0.16 mm; (d) Schematic diagram and optical microscope images of printed conductive sandwich structure, i) schematic diagram, ii) optical microscope image of top view, iii) optical microscope image of front view, iv) optical microscope image of enlarged conductive carbon cloth part in top view, v) optical microscope image of enlarged printing part in top view.

trend for the modulus of thermal-cured materials is the opposite. This is because in photocured materials, only the photosensitive part of the material cures, while the remaining thermosensitive part cures later to form the thermal-cured material. NVP, as a photosensitive material, leads to a higher modulus as its content increases due to more areas being cured in photocured materials. However, in fully cured materials, the modulus of the cross-linked material, bismaleimide, is higher than that of the linear material, NVP. Therefore, as the NVP content increases, the material modulus decreases. Nonetheless, the difference in modulus between materials with different NVP contents is not significant. This is because after thermal curing, both reactions of the material have already occurred, and the influence of NVP content on its modulus is minimal. Additionally, the elongation at break of the material slightly increases, due to the linear material NVP improving the flexibility of the material to a certain extent.

DMA is employed to assess the dynamic modulus of a thermally-cured material at room temperature, high temperature, and to determine its glass transition temperature. Fig. 5 (c) illustrates the DMA curves of materials with varying ratios. Notably, all materials with different compositions display shifts in storage modulus levels. Specifically, at the low-temperature plateau, the samples exhibit high modulus values, indicating a glassy state, while at the high-temperature plateau, the samples demonstrate low modulus values, indicative of a rubbery state. The sharp decrease in storage modulus between the two plateaus signifies a glass transition in the material, showcasing its shape memory effect. Analysis of the Tan δ curve reveals that materials with higher NVP content exhibit lower modulus levels and glass transition temperatures at the low-temperature plateau. This phenomenon aligns with the rationale behind the material's lower tensile modulus. The modulus of the materials remains below 40 MPa at 240 °C, and this temperature is chosen as the temperature for shape memory deformation. Compared with Fig. 3(c), the storage modulus of the thermo-cured resin was increased from 2528-3485 MPa to 4235–5229 MPa, and their T_g was increased from 80.1 to 108.8 ℃ to 178.2–187.4 ℃. The reason is same as the improvement in the mechanical properties of the resin mentioned above. The crosslink density of the resin obtained by using Equation (3)

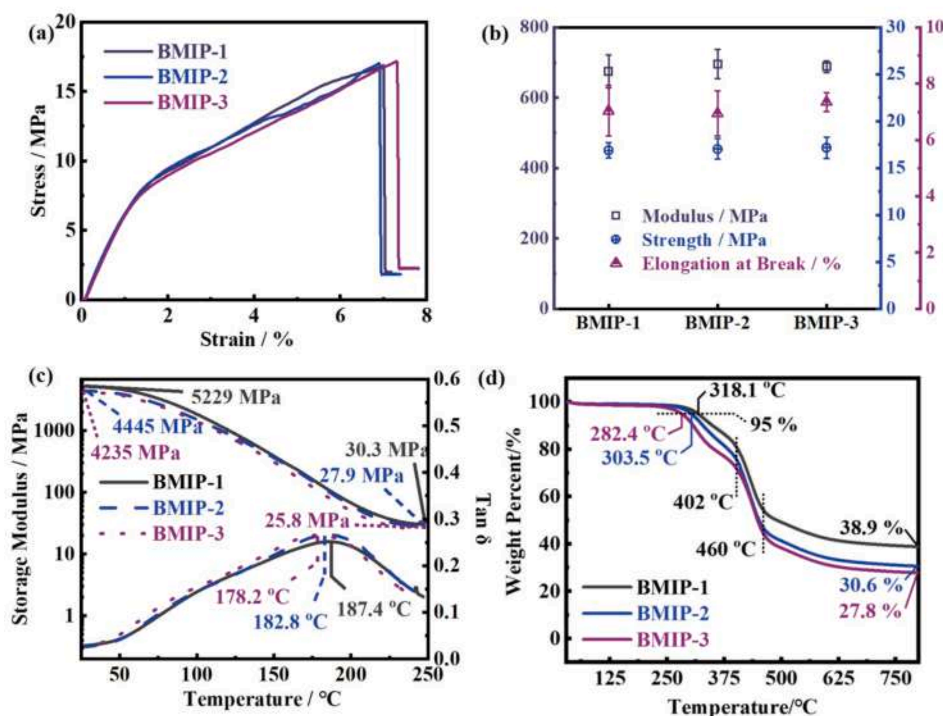

Fig. 5. Thermodynamic properties of printed materials with different compositions after thermal curing. (a) Stress–strain curves, (b) Summary of static mechanical properties, (c) DMA curves, (d) TGA curves under N_2 atmosphere.

was shown in Table S4. It can be seen that the crosslinking density of the resins calculated from the modulus of the rubbery state resins is in the range of 894.7–1711.1 mol/m^3. The higher the content of NVP, the higher the crosslinking density of the UV-cured resins. The crosslink density of the resin increases after heat curing. The higher the NVP content the lower the crosslinking density of the heat-cured resins.

The material's thermal stability was assessed through TGA, showing the thermal decomposition temperature and residual carbon content under N_2 atmosphere in Fig. 5(d). The thermal decomposition temperature (<5%) serves as an indicator of the operational temperature range for the material. Notably, the material exhibits a thermal decomposition temperature above 250 ℃ in a N_2 atmosphere, surpassing its deformation temperature, thus affirming excellent thermal stability. Residual carbon content fluctuates between 27.8 % to 37.9 %, with higher NVP content linked to reduced levels due to increased linear chain segments. As shown in Fig. S3, in an air atmosphere, initial weight loss is due to cross-linked network decomposition forming char, followed by subsequent oxidative char layer decomposition. Residual carbon content under air remains around 1 %, with a thermal decomposition temperature above 250 ℃, showcasing the material's ability to withstand shape memory cycles even in an air environment. And it is possible to realize self-healing process in air at 240 °C.

During the curing process, resins undergo dimensional shrinkage due to changes in atomic spacing. As the initiation temperature increases, the polymerization reaction occurs, shifting the intermolecular forces from van der Waals interactions to covalent bond formation. This results in a closer packing of atoms within the polymer, leading to dimensional shrinkage. Higher functionality of materials results in higher volume shrinkage after curing for materials with the same molecular weight. By designing a secondary curing process, the curing shrinkage rate can be effectively reduced. NVP undergoes photopolymerization under UV light, and during post-thermal curing, only BDM and DPS molecules have not reacted, reducing the functionality of the reactants, resulting in a smaller volume shrinkage during curing. Furthermore, materials with regular molecular structures, such as linear structures, exhibit larger volume shrinkage, while main chain molecules or crosslinking agents with branched or cyclic structures are influenced by the branched or cyclic structures during polymerization, leading to a decrease in curing shrinkage rate. Therefore, the NVP material selected in this study forms long chains with multiple branches after curing, while BDM and DPS contain maleimide rings and benzene rings, respectively, resulting in reduced curing shrinkage rate. The shrinkage rate of the materials in this study is characterized and compared with that of materials reported in other literature as shown in Fig. 6. Fig. 6(a) shows optical microscopic images of the material after thermal curing compared with Fig. 4(a-ii), where the surface morphology remains unchanged but shifts in color from yellow to reddish-brown. Fig. 6(b) demonstrates the dimensional changes of square-shaped materials before and after thermal curing. Fig. 6(c) presents images of materials with different printing patterns after thermal curing. By calculating the size changes between Fig. 6(c) and Fig. 4(b), the shrinkage rate of the structures printed by BMIP-2 was obtained. Measurements of the shrinkage before and after curing for materials with different ratios and patterns are summarized in Fig. 6(d), showing that the shrinkage rates are all less than 2 %, with a minimum of 0.21 %. BMIP-2 exhibited a slightly lower shrinkage rate compared to BMIP-1 and BMIP-3. The printed structures were printed by BMIP-2 resin, with a shrinkage rate similar to that of BMIP-2 and slightly lower than that of BMIP-1 and BMIP-3. A comparison of the shrinkage rates of the materials in this study with other printing materials, as well as their comparison with temperature and modulus data, is shown in Fig. 6(e) and 6(f), with more detailed information summarized in Table 2 [11,44–46,49–59]. Fig. 6(e) demonstrates that the material printed in this study has the lowest shrinkage rate and highest dynamic modulus among the various printing materials tested, indicating superior performance. Fig. 6(f) illustrates the comparison of T_g and shrinkage rate of different printing materials. Only PI materials exhibit a higher T_g than the material in this study. However, PI materials undergo significant shrinkage during curing, making them unsuitable for applications requiring precise dimensions. It is noteworthy that PLA, PCL, and PEEK are thermoplastic materials used in FFF printing with printing lines that essentially do not experience shrinkage. While these materials have low shrinkage rates, they are thermoplastic materials compared to the

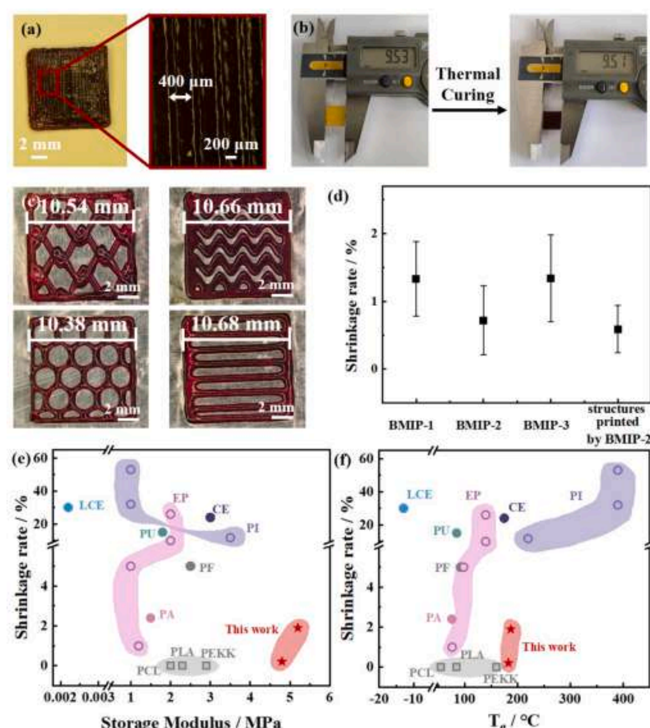

Fig. 6. (a) Optical microscope image of printed samples, (b) Measurement chart of shrinking rate of square object, (c) Photos of structures after curing with different patterns, (d) Shrinkage rates of materials with different ratios and structures, (e) – (f) Comparison charts of shrinking rate, temperature, and modulus between the material in this paper and other materials. (Square represents FFF printing, circle represents DLP or DIW printing). (PF for Phenol Formaldehyde, EP for Epoxy, CE for Cyanate Ester, LCE for Liquid Crystalline Elastomer, PU for Polyurethane, PCL for Poly(ε-caprolactone), PA for Polyacrylate, PLA for Polylactic Acid, PEKK for Poly Ether Ketone Ketone, PEEK for Poly Ether Ether Ketone, PI for Polyimide, NVP for N-Vinyl-Pyrrolidinone.).

thermal-cured material used in this study, resulting in significantly lower modulus and transition temperatures. Materials with low shrinkage rates are suitable for applications requiring precise dimensions, allowing for immediate use without the need for further processing or complex dimension adjustments.

3.5. Demonstration of multifunctional performance

The multifunctionality of materials has attracted increasing attention in recent years. This paper achieved a major breakthrough in multifunctional materials by combining high modulus, low shrinkage rate properties with self-healing, shape memory, electro-thermal deformation, and electro-thermal curing capabilities. The DPS molecule used in this study contains disulfide bonds, enabling the self-healing function of thermal-cured materials. The comparison curve of tensile properties before and after self-healing and the self-healing mechanism diagram are shown in Fig. S4. As a dynamic covalent bond, disulfide bonds undergo exchange at 240 ℃, achieving self-healing of small cracks on materials. Fig. S5 shows the stress relaxation curve of BMIP-2 at 240 ℃. It took less than 12 min for E/E_0 to decrease from 1 to 1/e, indicating that the material achieved dynamic covalent bond exchange within 12 min. This validated the self-healing mechanism of disulfide bonds as dynamic covalent bonds. By implementing a two-stage curing process, linear molecules were interleaved with crosslinked molecules to prepare semi-IPN polymers, endowing the materials with shape memory capabilities. Here, we characterized the shape memory performance of the materials. SMPs have the capability to undergo reversible deformation under stress. This is because such polymer materials are in a rubbery state at high temperatures, allowing molecular chains (soft segments) and crosslink points (hard segments) to move and rotate under external stress, enabling deformation. At low temperatures, the material is in a glassy state, where the crosslink points and molecular chains no longer move or rotate, thus preserving the shape. Upon reheating, the crosslink points return to their original positions, restoring the material to its initial shape. This shape memory mechanism can be achieved by adjusting the density of crosslink points and the structure of molecular chains. Shape fixity and shape recovery depend on the material's characteristics and the applied conditions. Shape fixity represents the material's ability to maintain a fixed shape during the shape memory process, and it is influenced by factors such as crosslink density, degree of interpenetration of molecular chains, and external structural limitations. Shape recovery reflects the material's ability to return to its original shape and is determined by its reversible deformation capacity. Shape fixity rate, shape recovery rate, and recovery time are quantitative parameters for characterizing shape memory performance. Fig. S1 shows the fixed angle and recovery angle of the bar sample, and Fig. S2

Table 2
Comparison table of modulus, shrinkage, printability, shape memory effect, self-healable, and T_g.

Material	Storage Modulus [GPa]	Shrinkage [%]	Prt	SME	SH	T_g [°C]	Ref
PF	1.5–2.5	5*	×	✓	×	78–92	[49]
EP	1.0	1–5*	×	✓	×	98	[50]
EP	1.2	1–5*	✓	✓	×	76.4	[51]
EP	2.0	9.9–26	✓	✓	×	140	[52]
CE	1.8–3.0	4–24	✓	✓	×	165–175	[53]
LCE	0.0022	10–50*	✓	✓	×	−12.9	[54]
PU	1.8	15	✓	×	×	85	[55]
PCL	1–2*	0* **	✓	✓	✓	55	[56]
PA	0.9–1.5	2.0–2.4*	✓	✓	×	48–76	[57]
PLA	2.3	0* **	✓	✓	×	85	[58]
PEKK6002	2.9	0* **	✓	×	×	143–160	[59]
PEEK	0.7–1.4	–	×	✓	×	171	[60]
PI	3.5	11–11.7	✓	×	×	220	[61]
PI	1.0	32–53	✓	×	×	390	[62]
NVP	2.0*	–	×	×	×	110	[52]
BMIP	4.2–5.2	0.21–1.98	✓	✓	✓	178.2–187.4	This work

Prt for Printability, SME for Shape Memory Effect, SH for Self-healable.
PF for Phenol Formaldehyde, EP for Epoxy, CE for Cyanate Ester, LCE for Liquid Crystalline Elastomer, PU for Polyurethane, PCL for Poly(ε-caprolactone), PA for Polyacrylate, PLA for Polylactic Acid, PEKK for Poly Ether Ketone Ketone, PEEK for Poly Ether Ether Ketone, PI for Polyimide, NVP for N-Vinyl-Pyrrolidinone.
* denotes estimated value.
** denotes the use of FFF printing technology for materials.

illustrates the process and time for the bar sample to recover its shape on a heating stage, from which the shape memory-related properties of different formulations and UV-cured samples were calculated and summarized in Table 1. It can be observed that the recovery rate of the UV-cured sample BMIP-2-UV is lower than that of the heat-cured samples, and the recovery time is longer. This is because the UV-cured sample only reacts with photosensitive molecules to form polymers, while the heat-cured molecules remain in a small molecule state. As a result, only the polymer part possesses “hard segments” and “soft segments,” and the combination of these segments determines the material’s recovery ability. After stress loading, the material is given a shape. Upon reheating, a synergistic interaction between the limited “hard segments” and “soft segments” enables the material to regain its original shape, while the remaining small molecule parts undergo free movement and lack the ability to recover the shape. Consequently, the recovery time of the material is longer, and the recovery rate is limited. After heat curing, it can be observed that the fixity and recovery rates of BMIP-1, BMIP-2, and BMIP-3 are all greater than 97 %. This is because after heat curing, the remaining small molecules of the material are also cured, resulting in an alternation of “hard segments” and “soft segments” in the material state. This leads to higher fixity and recovery rates, as well as faster recovery speed. Simultaneously, the interpenetration of linear polymer molecules and crosslinked polymer molecules in the semi-IPN structure provides better support for the material’s shape memory performance. The four times consecutive shape memory cycles was characterized by DMA, as shown in Fig. S6. It can be seen that materials with different ratios maintained good shape fixing rates and shape recovery rates after four shape memory cycles. Fig. 7 qualitatively demonstrates the shape memory process of the printed spring-pin structure. In the front view, the original shape of the structure shows the spring part in an expanded state, with one end of the spring connecting a block that protrudes compared to the outer shell of the structure. In the temporary shape, the spring part is compressed, and the block is retracted inside the outer shell of the structure. When the structure is placed in an oven, the spring part gradually extends, and the block gradually emerges from the outer shell, enabling the function of a pin. In the side view, the two misaligned circular notches in the original shape of the structure become aligned in the temporary shape, allowing objects to be placed in the notches for locking. As the structure is placed in the oven, the spring part of the structure recovers, the notches gradually misalign, and the objects to be locked are secured. Therefore, this structure, in the shape memory process, can achieve the functions of pinning and locking, making it applicable in scenarios requiring such functions.

In this study, by printing a sandwich structure on a conductive substrate and controlling its electrical conductivity and voltage, the reconfigurability of shape memory composite structures was achieved through a process of initial shape memory deformation, in-situ self-limiting resistive heating for secondary curing, and subsequent shape memory deformation. This process was demonstrated in Fig. 8. Fig. 8(a)

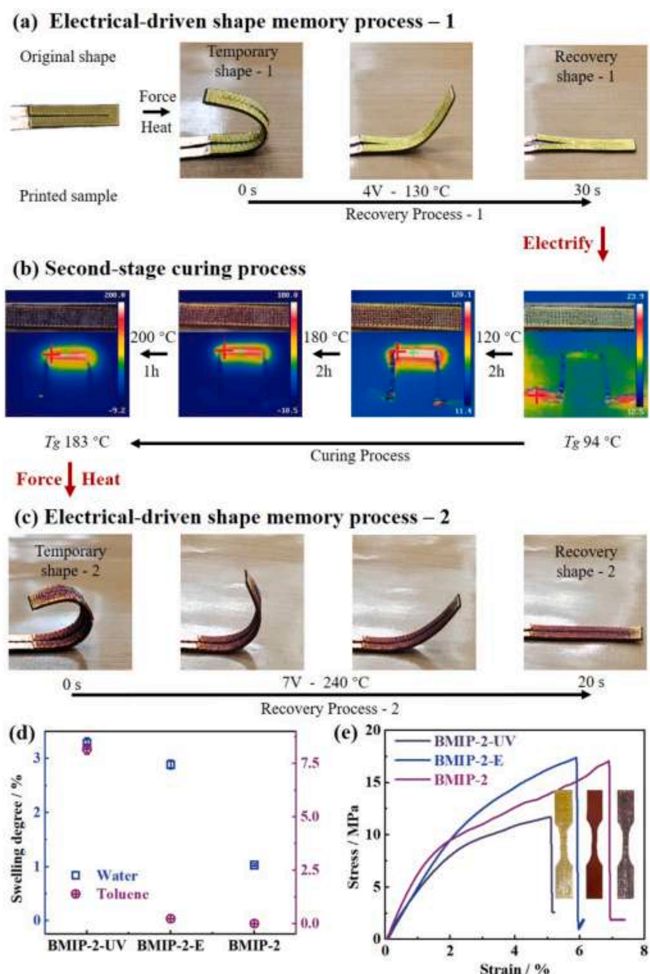

Fig. 8. (a) Electrical-driven shape memory process of printed conductive sandwich structure, (b) Second-stage curing process of electrical-heated printed conductive sandwich structure, (c) Electrical-driven shape memory process of printed conductive sandwich structure after thermal curing, (d) Swelling degree data of UV-cured samples, electrical-cured samples, and thermal-cured samples, (e) Tensile curves of UV-cured samples, electrical-cured samples, and thermal-cured samples.

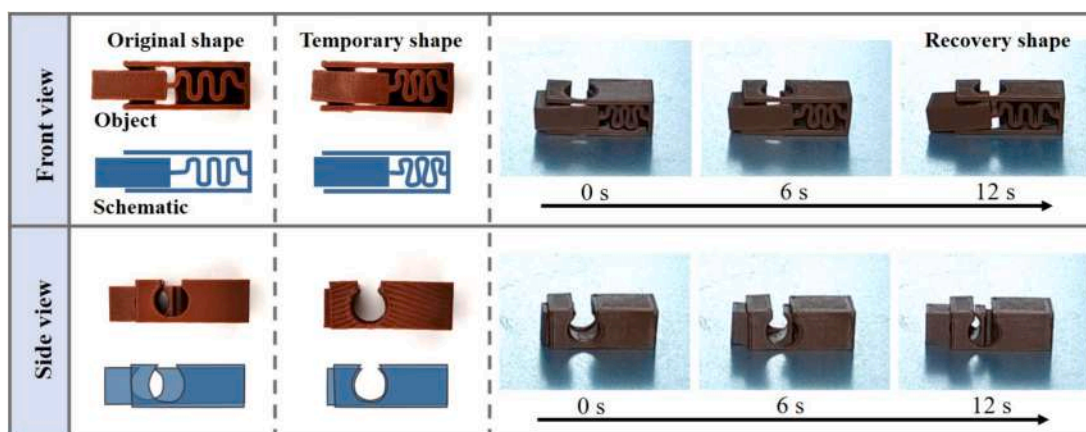

Fig. 7. Shape memory process of printed spring-pin structure.

illustrates the process of shape memory upon electrical-driven of the printed conductive sandwich structure. The conductive carbon fabric was printed on both sides to obtain a sample that had only undergone photocuring treatment, maintaining its original shape. As mentioned earlier, the material's T_g at this stage was 94 °C. The sandwich structure was shaped into a U shape at high temperatures and subsequently cooled to room temperature, thus imparting a fixed temporary shape − 1. Subsequently, the electrodes at both ends were connected to a DC power supply, with the voltage was being tuned to around 4 V. At this stage, the temperature of the structure was measured at 130 °C, causing the U-shaped structure to gradually unfold into a planar structure, recovering shape − 1. Fig. 8(b) shows the second-stage curing process during electrical-heating of the printed conductive sandwich structure. By adjusting the voltage, the temperature of the conductive sandwich structure gradually increased, and the curing process was similar to conventional oven heat curing, with the material's color transitioning from yellow to reddish-brown, achieving in-situ self-limiting resistive heating curing. As mentioned earlier, the material's T_g at this stage was 183 °C. The resistance of the conductive sandwich structure before and after curing were 14.1 Ω and 14.4 Ω, respectively. The optical microscope images of sandwich structures cured by electrical-heating were shown in Fig. S7. Fig. 8(c) illustrates the process of shape memory upon electrical-heating of the printed conductive sandwich structure after thermal curing. Similar to the photocured sample, the sandwich structure was shaped into a U shape at high temperatures, then cooled to room temperature, thereby fixing the shape as temporary shape − 2. Applying around 7 V of voltage heated the sample to 240 °C, causing the U-shaped structure to gradually unfold into a planar structure, recovering shape − 2. This successfully demonstrated the reconfigurability of the conductive sandwich structure through the process of initial shape memory deformation, followed by in-situ self-limiting resistive heating secondary curing, and subsequent shape memory deformation. The cured samples were quantitatively analyzed and compared against photocured and thermally cured samples. Fig. 8S showed the swelling degree − time curves of photo-cured samples, electrical-cured samples, and thermal-cured samples. The data was summarized in Fig. 8(d), showing that the swelling degree of the electrical-cured samples was comparable to that of the thermal-cured samples, indicating similar crosslinking densities and suggesting that electrical-curing is a feasible method comparable to thermal curing. The higher swelling of the photocured samples compared to the electrical-cured and thermal-cured samples indicates lower crosslinking density due to incomplete reaction of BDM and DPS in the photocured samples. Fig. 8(e) shows the tensile curves of the photocured, electrical-cured, and thermal-cured samples, indicating that the modulus, strength, and elongation values of the electrical-cured and thermal-cured samples were similar, suggesting similar properties. The photocured samples, with incomplete reaction, exhibited lower modulus, strength, and elongation compared to the electrical-cured and thermal-cured samples. The in-situ self-limiting resistive heating and secondary shape memory deformation reconfigurable process offer more possibilities for the development of deformable structures in the aerospace field. However, the limitations of this multifunctional structure are similar to those of shape memory materials. After curing by electrical heating, the structure can undergo the process of shape memory again, but the realization of this process is still based on the external force to shape the structure again.

Finally, in addition to comparing the modulus, T_g, and shrinkage as described earlier, we also compared whether the materials can be printed, whether they exhibit shape memory effects, and whether they have self-healing capabilities, and summarized these data in Table 2. It can be seen that the BMIP material prepared in this study has the highest energy storage modulus, the lowest shrinkage (excluding materials printed with FFF), the highest T_g (excluding PI), and simultaneously possesses various functions such as printability, shape memory effects, and self-healing capabilities among the materials listed in Table 2. It represents a novel advanced material in the field of 4D printing that combines high performance and multifunctionality. This advanced material has laid a solid foundation for in-orbit printing in space.

4. Conclusions

In response to the limited variety and properties of 4D printing materials, we propose a 4D printable maleimide-based material with high storage modulus, low shrinkage, and high transition temperature advantages. By introducing the photosensitive molecule NVP, which also acts as a diluent, and mixing it with BDM and DPS molecules, a printable resin is obtained. The synthesis process is conducted using a one-pot method, which is simple, efficient, and environmentally friendly. Subsequently, by designing a two-step curing process to reduce the reactivity of functional groups and selecting molecules with low linearity, the material achieves a high storage modulus of 5229 MPa and a low shrinkage rate of 0.21 %. Moreover, the introduction of disulfide bonds enables the thermosetting material with self-healing capabilities, achieving repair efficiencies exceeding 71 %. Furthermore, by printing a sandwich structure on a conductive substrate and adjusting its current and voltage, the reconfigurable capability of the composite material structure is achieved. This involves initiating shape memory deformation first, followed by in-situ self-locking, electrothermal secondary curing, and then further shape memory deformation. This advancement lays a solid foundation for in-orbit printing and provides more possibilities for the development of deformable structures in the aerospace field through the processes of electro-thermal curing and secondary deformation.

CRediT authorship contribution statement

Yuejia Li: Writing – review & editing, Writing – original draft, Visualization, Methodology, Investigation, Data curation. **Fenghua Zhang:** Writing – review & editing, Validation, Resources, Project administration, Methodology, Investigation. **Yanju Liu:** Supervision, Project administration, Funding acquisition, Conceptualization. **Jinsong Leng:** Writing – review & editing, Supervision, Project administration, Funding acquisition, Conceptualization.

Declaration of competing interest

The authors declare that they have no known competing financial interests or personal relationships that could have appeared to influence the work reported in this paper.

Data availability

No data was used for the research described in the article.

Acknowledgements

We thank National Key R&D Program of China (2022YFB3805700) and National Nature Science Foundation of China (Grant No. 92271112 and 92271206) for the support of this work.

Appendix A. Supplementary data

Supplementary data to this article can be found online at https://doi.org/10.1016/j.cej.2024.152196.

References

[1] M. Behl, A. Lendlein, Shape-memory polymers, Mater. Today. 10 (4) (2007) 20–28, https://doi.org/10.1016/S1369-7021(07)70047-0.

[2] S. Yan, F. Zhang, L. Luo, L. Wang, Y. Liu, Jinsong Leng, Shape Memory Polymer Composites: 4D Printing, Smart Structures and Applications, *Research* 6 (2023) 0234, https://doi.org/10.34133/research.0234.

[3] L. Yu, H. Yu, Light-powered tumbler movement of graphene oxide/polymer nanocomposites, ACS Appl. Mater. Interfaces. 7 (6) (2015) 3834–3839, https://doi.org/10.1021/am508970k.

[4] Y. Li, H. Chen, D. Liu, W. Wang, Y. Li, S. Zhou, pH-Responsive Shape Memory Poly (ethylene glycol)-Poly(epsilon-caprolactone)-based polyurethane/cellulose nanocrystals nanocomposite, ACS Appl. Mater. Interfaces. 7 (23) (2015) 12988–12999, https://doi.org/10.1021/acsami.5b02940.

[5] L. Luo, F. Zhang, J. Leng, Shape memory epoxy resin and its composites: from materials to applications, Research (2022) 9767830, https://doi.org/10.34133/2022/9767830.

[6] Y. Li, W. Pan, F. Zhang, J. Leng, Shape memory polyimide composites with high storage modulus and high glass transition temperature, J. Intel. Mater. Syst. Struct. 33 (14) (2021) 1762–1772, https://doi.org/10.1177/1045389X211064347.

[7] K. Mirasadi, D. Rahmatabadi, I. Ghasemi, M. Khodaei, M. Baniassadi, M. Baghani, Investigating the effect of ABS on the mechanical properties, morphology, printability, and 4D printing of PETG - ABS blends, Macromol. Mater. Eng. 2400038 (2024), https://doi.org/10.1002/mame.202400038.

[8] D. Rahmatabadi, K. Soltanmohammadi, M. Aberoumand, E. Soleyman, I. Ghasemi, M. Baniassadi, K. Abrinia, M. Bodaghi, M. Baghani, 4D printing of porous PLA-TPU structures: effect of applied deformation, loading mode and infill pattern on the shape memory performance, Phys. Scr. 99 (2) (2024) 025013, https://doi.org/10.1088/1402-4896/ad1957.

[9] D. Rahmatabadi, M. Aberoumand, K. Soltanmohammadi, E. Soleyman, I. Ghasemi, M. Baniassadi, K. Abrinia, M. Bodaghi, M. Baghani, Toughening PVC with biocompatible PCL softeners for supreme mechanical properties, morphology, shape memory effects, and FFF printability, Macromol. Mater. Eng. 308 (10) (2023) 2300114, https://doi.org/10.1002/mame.202300114.

[10] Y. Li, F. Zhang, Y. Liu, J. Leng, Programmable shape memory bismaleimide composite claw with two-way grabbing function, Comp. a. 165 (2023) 107328, https://doi.org/10.1016/j.compositesa.2022.107328.

[11] I.J. Robert, W. Carwyn, H. Ian, Modern advances in bismaleimide resin technology: A 21st century perspective on the chemistry of addition polyimides, Prog. Polym. Sci. 69 (2017) 1–21, https://doi.org/10.1016/j.progpolymsci.2016.12.002.

[12] Y. Yang, Y. Wang, T. Yao, X. Feng, A flexible and smart shape memory alloy composite sheet based on efficient and bidirectional thermal management, Intel. J. Smart. Nano. Mater. 13 (2) (2022) 315–329, https://doi.org/10.1080/19475411.2022.2076754.

[13] B. Tian, X. Jiang, W. Chu, C. Zheng, W. Guo, Z. Zhang, Integrating reduced graphene oxides and PPy nanoparticles for enhanced electricity from water evaporation, Intel. J. Smart. Nano. Mater. 14 (2) (2023) 230–242, https://doi.org/10.1080/19475411.2023.2205176.

[14] H. Yang, Z. Zhou, J. Ou, A novel smart steel strand based on optical-electrical co-sensing for full-process and full-scale monitoring of prestressing concrete structures, Intel. J. Smart. Nano. Mater. 14 (3) (2023) 337–368, https://doi.org/10.1080/19475411.2023.2237940.

[15] H. Cao, R. Xu, D. Yu, Thermal and dielectric properties of bismaleimide-triazine resins containing octa(maleimidedophenyl)silsesquioxane, J. Appl. Polym. Sci. 109 (5) (2008) 3114–3121, https://doi.org/10.1002/app.27822.

[16] R.K. Jena, C.Y. Yue, M.M. Sk, K. Ghosh, A novel high performance bismaleimide/diallyl bisphenol A (BMI/DBA)-epoxy interpenetrating network resin for rigid riser application, RSC. Adv. 5 (97) (2015) 79888–79897, https://doi.org/10.1039/c5ra14474d.

[17] P. Musto, E. Martuscelli, G. Ragosta, P. Russo, G. Scarinzi, An interpenetrated system based on a tetrafunctional epoxy resin and a thermosetting bismaleimide: structure-Properties correlation, J. Appl. Polym. Sci. 69 (5) (1998) 1029–1042, https://doi.org/10.1002/(SICI)1097-4628(19980801)69:5<1029::AID-APP23>3.3.CO;2-Q.

[18] C. Gouri, C.P.R. Nair, R. Ramaswamy, K.N. Ninan, Thermal decomposition characteristics of Alder-ene adduct of diallyl bisphenol A novolac with bismaleimide: effect of stoichiometry, novolac molar mass and bismaleimide structure, Eur. Pold. J. 38 (2002) 503–510, https://doi.org/10.1016/S0014-3057(01)00197-5.

[19] Y. Li, F. Zhang, Y. Liu, J. Leng, A tailorable series of elastomeric-to-rigid, selfhealable, shape memory bismaleimide, Small 2307244 (2023), https://doi.org/10.1002/smll.202307244.

[20] F. Momeni, N.S.M. Hassani, X. Liu, J. Ni, A review of 4D printing, Mater. Des. 122 (2017) 42–79, https://doi.org/10.1016/j.matdes.2017.02.068.

[21] S.K. Leist, J. Zhou, Current status of 4D printing technology and the potential of light-reactive smart materials as 4D printable materials, Virtual Phys. Prototype 11 (2016) 249–262, https://doi.org/10.1080/17452759.2016.1198630.

[22] Z.X. Khoo, J.E.M. Teoh, Y. Liu, C. Chua, S. Yang, J. An, K. Leong, W. Yeong, 3D printing of smart materials: A review on recent progresses in 4D printing, Virtual Phys Protot 10 (2015) 103–122, https://doi.org/10.1080/17452759.2015.1097054.

[23] D. Shin, T. Kim, D. Kim, Review of 4D printing materials and their properties, Int. J Precis. Eng. Manuf-Green. Tech. 4 (2017) 349–357, https://doi.org/10.1007/s40684-017-0040-z.

[24] Q. Ge, A.H. Sakhaei, H. Lee, C.K. Dunn, N. Fang, M.L. Dunn, Multimaterial 4D printing with tailorable shape memory polymers, Sci. Rep. 6 (2016) 31110, https://doi.org/10.1038/srep31110.

[25] A. Lee, J. An, C. Chua, Two-way 4D printing: A review on the reversibility of 3D-printed shape memory materials, Engineering 3 (2017) 663–674, https://doi.org/10.1016/J.ENG.2017.05.014.

[26] M. Bodaghi, A.R. Damanpack, W, Liao, Adaptive metamaterials by functionally graded 4D printing, Mater. Des. 135 (2017) 26–36, https://doi.org/10.1016/j.matdes.2017.08.069.

[27] J. Choi, O. Kwon, W. Jo, H. Lee, M. Moon, 4D printing technology: A review, 3D Print Add Manuf. 2 (2015) 159–167, https://doi.org/10.1089/3dp.2015.0039.

[28] M. Bodaghi, A.R. Damanpack, W.H. Liao, Triple shape memory polymers by 4D printing, Smart Mater. Struct. 27 (2018) 065010, https://doi.org/10.1088/1361-665X/aabc2a.

[29] S.T. Ly, J.Y. Kim, 4D printing-Fused deposition modeling printing with thermal-responsive shape memory polymers, Int. J. Precis. Eng. Manuf. Green. Tech. 4 (2017) 267–272, https://doi.org/10.1088/1361-665X/aabc2a.

[30] Y. Yang, Y. Chen, Y. Wei, Y. Li, 3D printing of shape memory polymer for functional part fabrication, Int. J. Adv. Manuf. Technol. 84 (2016) 2079–2095, https://doi.org/10.1002/adma.201701627.

[31] S. Miao, N. Castro, M. Nowicki, L. Xia, H. Cui, X. Zhou, W. Zhu, S. Lee, K. Sarkar, G. Vozzi, Y. Tabata, J. Fisher, L. Zhang, 4D printing of polymeric materials for tissue and organ regeneration, Mater. Today. 20 (2017) 577–591, https://doi.org/10.1016/j.mattod.2017.06.005.

[32] L. Huang, R. Jiang, J. Wu, J. Song, H. Bai, B. Li, Q. Zhao, T. Xie, Ultrafast digital printing toward 4D shape changing materials, Adv. Mater. 29 (2017) 1605390, https://doi.org/10.1002/adma.201605390.

[33] X. Li, J. Shang, Z. Wang, Intelligent materials: A review of applications in 4D printing, Assem. Automat. 37 (2017) 170–185, https://doi.org/10.1108/AA-11-2015-093.

[34] E. Pei, 4D Printing: dawn of an emerging technology cycle, Assem. Automat. 34 (2014) 310–314, https://doi.org/10.1108/AA-07-2014-062.

[35] Y.Y.C. Choong, S. Maleksaeedi, H. Eng, J. Wei, P. Su, 4D printing of high-performance shape memory polymer using stereolithography, Mater. Des. 126 (2017) 219–225, https://doi.org/10.1016/j.matdes.2017.04.049.

[36] M.D. Monzón, R. Paz, E. Pei, F. Ortega, L.A. Suárez, Z. Ortega, M.E. Alemán, T. Plucinski, N. Clow, 4D printing: Processability and measurement of recovery force in shape memory polymers, Int. J. Adv. Manuf. Technol. 89 (2017) 1827–1836, https://doi.org/10.1007/s00170-016-9233-9.

[37] S. Naficy, R. Gately, I.R. Gorkin, H. Xin, G.M. Spinks, 4D printing of reversible shape morphing hydrogel structures, Macromol. Mater. Eng. 302 (2017) 1600212, https://doi.org/10.1002/mame.201600212.

[38] Y. Li, F. Zhang, Y. Liu, J. Leng, 4D printed shape memory polymers and their structures for biomedical applications, Sci. China. Techol. Sci. 63 (4) (2020) 545–560, https://doi.org/10.1007/s11431-019-1494-0.

[39] X. Wan, H. Wei, F. Zhang, Y. Liu, J. Leng, 3D printing of shape memory poly (d, l-lactide-co-trimethylene carbonate) by direct ink writing for shape-changing structures, J. Appl. Polym. Sci. 48177 (2019), https://doi.org/10.1002/app.48177.

[40] K. Kim, W. Zhu, X. Qu, C. Aaronson, W.R. McCall, S. Chen, D.J. Sirbuly, 3D optical printing of piezoelectric nanoparticle-polymer composite materials, ACS Nano 8 (10) (2014) 9799–9806, https://doi.org/10.1021/nn503268f.

[41] Q. Mu, C.K. Dunn, L. Wang, M.L. Dunn, H.J. Qi, T. Wang, Thermal cure effects on electromechanical properties of conductive wires by direct ink write for 4D printing and soft machines, Smart Mater. Struct. 26 (4) (2017) 045008, https://doi.org/10.1088/1361-665X/aa5cca.

[42] C. Yoon, R. Xiao, J. Park, J. Cha, T.D. Nguyen, D.H. Gracias, Functional stimuli responsive hydrogel devices by self-folding, Smart Mater. Struct. 23 (9) (2014) 094008, https://doi.org/10.1088/0964-1726/23/9/094008.

[43] T.G. Leong, C.L. Randall, B.R. Benson, N. Bassik, G.M. Stern, D.H. Gracias, Tetherless thermobiochemically actuated microgrippers, Proc. Natl. Acad. Sci. 106 (3) (2009) 703–708, https://doi.org/10.1073/pnas.0807698106.

[44] X. Lan, X. Wang, Y. Liu, J. Leng, Fiber reinforced shape-memory polymer composite, its application in a deployable hinge, Smart Mater. Struct. 18 (2009) 024002, https://doi.org/10.1117/12.775760.

[45] B. Myers, M. Bernardi, J.C. Grossman, Three-dimensional photovoltaics, Appl. Phys. Lett. 96 (7) (2010) 071902, https://doi.org/10.1063/1.3308490.

[46] X. Guo, H. Li, B.Y. Ahn, E.B. Duoss, K.J. Hsia, J.A. Lewis, R.G. Nuzzo, Two-and three-dimensional folding of thin film single-crystalline silicon for photovoltaic power applications, Proc. Natl. Acad. Sci. 106 (48) (2009) 20149–20154, https://doi.org/10.1073/pnas.0907390106.

[47] B.A. Saville, A.A. Watson, Structural characterization of sulfur - vul- canized rubber networks, Rubber Chem. Technol. 40 (1) (1967) 100–148, https://doi.org/10.5254/1.3539039.

[48] R. Hagen, L. Salman, B. Stenberg, Effects of the type of crosslink on viscoelastic properties of natural rubber, J. Polym. Sci. Part b: Polym. Phys. 34 (12) (1996) 1997–2006, https://doi.org/10.1002/(SICI)1099-0488(19960915)34:12<1997::AID-POLB5>3.0.CO;2-N.

[49] L. Hu, F. Zhang, L. Luo, L. Wang, Y. Liu, J. Leng, Design and preparation of shape memory phenol-formaldehyde foam composites with excellent thermal stability and mechanical properties, Comp. A 174 (2023) 107738, https://doi.org/10.1016/j.compositesa.2023.107738.

[50] H. Zhao, X. Lan, L. Liu, Y. Liu, J. Leng, Design and analysis of shockless smart releasing device based on shape memory polymer composites, *Comp. Struct.* 223 (2019) 110958, https://doi.org/ 10.1016/j.compstruct.2019.110958.

[51] K. Chen, X. Kuang, V. Li, G. Kang, H.J. Qi, Fabrication of tough epoxy with shape memory effects by UV-assisted direct-ink write printing, Soft Matter 14 (2018) 1879, https://doi.org/10.1039/c7sm02362f.

[52] X. Kuang, Z. Zhao, K. Chen, D. Fang, G. Kang, H.J. Qi, High-speed 3D printing of high-performance thermosetting polymers via two-stage curing, Macromol. Rapid Commun. 39 (7) (2018) 1700809, https://doi.org/10.1002/marc.201700809.

[53] Z. Tang, J. Gong, P. Cao, L. Tao, X. Pei, T. Wang, Y. Zhang, Q. Wang, J. Zhang, 3D printing of a versatile applicability shape memory polymer with high strength and high transition temperature, Chem. Eng. J. 431 (2022) 134211, https://doi.org/10.1016/j.cej.2021.134211.

[54] Y. Xia, T. Mu, Y. He, Y. Liu, J. Leng, Fiber-reinforced liquid crystalline elastomer composite actuators with multi-stimulus response properties and multi-directional morphing capabilities, Comp. B 256 (2023) 110640, https://doi.org/10.1016/j.compositesb.2023.110640.

[55] T. Zhao, R. Yu, X. Li, B. Cheng, Y. Zhang, X. Yang, X. Zhao, Y. Zhao, W. Huang, 4D printing of shape memory polyurethane via stereolithography, Eur. Polym. J. 101 (2018) 120–126, https://doi.org/10.1016/j.eurpolymj.2018.02.021.

[56] J. Wen, T. Chen, J. Wang, X. Tuo, Y. Gong, J. Guo, Study on the healing performance of poly(ε-caprolactone) filled ultraviolet-curable 3D printed cyclic trimethylolpropane formal acrylate shape memory polymers, J. Appl. Poly. Sci. 139 (44) (2022) 53085, https://doi.org/10.1002/app.53085.

[57] H. Wu, P. Chen, C. Yan, C. Cai, Y. Shi, Four-dimensional printing of a novel acrylate-based shape memory polymer using digital light processing, Mater. Des. 175 (2019) 107704, https://doi.org/10.1016/j.matdes.2019.107704.

[58] X. Dong, F. Zhang, L. Wang, Y. Liu, J. Leng, 4D printing of electroactive shape-changing composite structures and their programmable behaviors, Comp. A 157 (2022) 106925, https://doi.org/10.1016/j.compositesa.2022.106925.

[59] K. Rodzen, A. McIlhagger, B. Strachota, A. Strachota, B.J. Meenan, A. Boyd, Controlling Crystallization: A Key Factor during 3D Printing with the Advanced Semicrystalline Polymeric Materials PEEK, PEKK 6002, and PEKK 7002, Macromol. Mater. Eng. 308 (2023) 2200668, https://doi.org/10.1002/mame.202200668.

[60] S. Yang, Y. He, Y. Liu, J. Leng, Efficient voltage actuators based on rapid heat and electric dual-response poly(aryl ether ketone) shape memory composites reinforced with radially aligned CNTs, Comp. A 158 (2022) 106940, https://doi.org/10.1016/j.compositesa.2022.106940.

[61] J. Zhang, Y. Zhang, L. Tao, T. Wang, Q. Wang, Integrated printing of high-strength, high-shape-retaining polyimide and its composite gradient structures for enhanced tribological properties, Addit. Manuf. 65 (2023) 103440, https://doi.org/10.1016/j.addma.2023.103440.

[62] M. Hegde, V. Meenakshisundaram, N. Chartrain, S. Sekhar, D. Tafti, C.B. Williams, T.E. Long, 3D Printing All-Aromatic Polyimides using Mask-Projection Stereolithography: Processing the Nonprocessable, Adv. Mater. 29 (31) (2017) 1701240, https://doi.org/10.1002/adma.201701240.